Using GNSS Signals as a Proxy for SAR Signals: Correcting Ionospheric Defocussing

Mannix, Chris; Belcher, David; Cannon, P.S.; Angling, Matthew

DOI:
10.1002/2015RS005822

AGU PUBLICATIONS

Radio Science

RESEARCH ARTICLE
10.1002/2015RS005822

Key Points:
- GNSS carrier amplitude and phase can be used to synthesize the SAR point spread function
- Two position GNSS measurements can be used to test mitigation of ionospheric effects on SAR
- Corrections can be made over a distance of ~3 km in the ionosphere (~6 km on the ground)

Correspondence to:
P. S. Cannon,
p.cannon@bham.ac.uk

Citation:
Mannix, C. R., D. P. Belcher, P. S. Cannon, and M. J. Angling (2016), Using GNSS signals as a proxy for SAR signals: Correcting ionospheric defocusing, *Radio Sci.*, *51*, doi:10.1002/2015RS005822.

Received 3 OCT 2015
Accepted 18 DEC 2015
Accepted article online 28 DEC 2015

Using GNSS signals as a proxy for SAR signals: Correcting ionospheric defocusing

Christopher R. Mannix[1], David P. Belcher[1], Paul S. Cannon[1], and Matthew J. Angling[1]

[1]School of Electronic, Electrical and Systems Engineering, University of Birmingham, Birmingham, UK

Abstract Ultrahigh frequency space-based synthetic aperture radar (SAR) can suffer from the degrading effects of a scintillating ionosphere which modulates both the phase and the amplitude of the radar signal. In this paper, we use Global Navigation Satellite System (GNSS) signals to synthesize an L-band SAR point spread function (PSF). The process of transforming the GNSS signal to the equivalent SAR PSF is described. The synthesized PSF is used to explore the possibility of using a phase correction determined from a point target in a SAR image to correct the ionospheric degradation. GNSS data recorded on equatorial Ascension Island during scintillation events are used to test the feasibility of this approach by applying a phase correction to one GNSS receiver from another located along a magnetic east-west baseline. The peak-to-sidelobe ratios of the synthesized L-band SAR point spread functions before and after the correction are compared, and it is shown that this approach improves the L-band PSF over distances of ~3000 m in the ionosphere, corresponding to 6000 m on the ground.

1. Introduction

Space-based (SB) synthetic aperture radar (SAR) can provide high-resolution, all-weather ground imaging. However, those radars which operate at or below L-band can be seriously compromised by propagation through the ionosphere [*Quegan and Lamont*, 1986]. Two categories of ionospheric effect are commonly identified—those associated with Faraday rotation of the polarization vector [*Meyer and Nicoll*, 2008] and those associated with small- and medium-scale electron density irregularities which impose variations on the signal amplitude [*Belcher and Cannon*, 2014] and on the signal phase [*Xu et al*., 2004; *Cannon*, 2009]. The irregularity-induced effects are commonly referred to as ionospheric scintillation and are due to diffraction and refraction of the signal.

The ionospheric irregularities can be described by a spatial power spectrum, which follows a power law between two characteristic scales sizes—the inner scale size (the electron gyroradius, ~2 cm) and the outer scale size (~10–50 km) [*Yeh et al*., 1975; *Rino*, 1982]. Given that the sizes of the irregularities are both smaller and comparable to the synthetic aperture of L-band SB-SARs (typically 10–20 km), both systematic and random phase changes can be introduced across the synthetic aperture. These ionospheric phase changes reduce the signal coherency, and once the size of the phase variations reaches ~$\pi/4$ rads, image reconstruction is severely affected [*van de Kamp et al*., 2009] unless autofocus techniques can be successfully employed [*Knepp and Groves*, 2011]. Among other effects, phase scintillation reduces the image contrast and if sufficiently strong can defocus SB-SAR images. *Rino and Gonzalez* [1983] provide evidence for these effects in the high latitudes, and similar effects have recently been shown at low latitudes [*Belcher et al*., 2015].

It is clearly desirable to quantify these effects, yet there are few L-band radars and even fewer coordinated SB-SAR and ionospheric measurements. This work seeks to circumvent this problem by developing a technique to quantify ionospheric scintillation effects on L-band SB-SAR based on widely available L-band Global Navigation Satellite System (GNSS) signals [*Aarons et al*., 1996; *Pi et al*., 1997]. Although the work described here is applicable to all GNSS constellations, the results presented use Global Positioning System (GPS) data only, and henceforth, the term GPS rather than the more general GNSS will be used.

In section 2, an approach to synthesize L-band SB-SAR signals from GPS signals is developed and the limitations of using this proxy data are explained. Then in sections 4 and 5, using data from an experiment described in section 3, a number of analyses are described which build upon each other. First, in section 4, proxy point spread functions (PSFs) are calculated and shown to possess the expected characteristics. Then, in section 5, GPS data simultaneously collected on two receivers are used to determine over what distance

a measurement of the PSF at one location can be used to sharpen the PSF (and consequently the image) at another location.

In this paper reference will be made to the PALSAR-2 radar [*Kankaku et al.*, 2013] which was launched in 2014. It operates at L-band and provides 5 m resolution in strip-map mode and up to 1 m resolution in spotlight mode.

2. Theory

2.1. The Phase Spectrum

As radio frequency signals propagate through the ionosphere, they experience a phase shift due to the electron content along the signal path. This is determined by the three-dimensional distribution of electrons which, for weak scattering, is well modeled as one or more horizontal two-dimensional thin phase screens by integrating the electron distribution in the vertical direction [*Rino*, 1979; *Knepp*, 1983]. The phase shift is assumed to occur at the ionospheric pierce point (IPP), where the ray intersects the screen.

For nongeosynchronous satellites, the raypath scans the phase screen and the resultant temporal variation can be represented as a (phase) power spectral density (PSD) [*Rino*, 1979]:

$$\mathrm{PSD}_{\phi}(f) = T\left(f_o^2 + f^2\right)^{-\frac{p}{2}}, \tag{1}$$

where f is the spectral frequency, f_o is the outer scale frequency, T is a constant, and p is the phase spectral index. The latter lies between 1 and 4 and is typically ~2.5 [*Basu et al.*, 1987].

This temporal spectrum can be transformed to the spatial domain [*Belcher and Rogers*, 2009] to give

$$\mathrm{PSD}_{\phi}(\kappa) = T'\left(\kappa_o^2 + \kappa^2\right)^{-\frac{p}{2}}, \tag{2}$$

where $\kappa = \frac{2\pi}{x}$ is the spatial wave number, x is the distance along the phase screen, and T' is given by

$$T' = \frac{r_e^2 \lambda^2 G C_s L \sec\theta \sqrt{\pi}\Gamma\left(\frac{p}{2}\right)}{4\pi^2 \Gamma\left(\frac{p+1}{2}\right)}. \tag{3}$$

Here r_e is the classical electron radius, λ is the wavelength of the signal, G is a factor that depends on the propagation geometry, C_s is the three-dimensional strength of the ionospheric turbulence, L is the effective thickness of the ionosphere, θ is the zenith angle, and Γ represents the Gamma function.

The root-mean-square (RMS) phase variation over a distance L_C along the phase screen (with κ_C as the associated spatial wave number) is obtained by integrating equation (2) over all spatial wave numbers above κ_C. To simplify the integral, the assumption $\kappa_0 \ll \kappa$ has been made, being appropriate to many of the spatial scales relevant to this work:

$$\phi_{\mathrm{RMS}}^2 \simeq \frac{2T'}{p-1} \kappa_C^{1-p}. \tag{4}$$

2.2. The Point Spread Function

This work will make much use of the point spread function (PSF) which describes the response of an imaging system to a point target and provides insight into the eventual quality of the images. It can be quantified by the peak-to-sidelobe ratio (PSLR).

For PALSAR the PSLR is defined as the ratio of the peak sidelobe intensity to the intensity of the main lobe, considering only the sidelobes within ±10 resolution cells of the main lobe [*Vexcel Corporation*, 2003].

$$\mathrm{PSLR}\ (d\mathrm{B}) = 10\log_{10}\frac{I_{\mathrm{PSL}}}{I_{\mathrm{ML}}}\ . \tag{5}$$

2.3. Effect of the Ionosphere on the SAR PSF

The along-track point spread function of a SAR system—assuming no degradation by the propagation medium—can be measured by imaging a point target, such as a trihedral corner reflector (CR) [*Freeman*, 1992]. However, as the radar moves in the along-track direction, the raypath traverses the time-varying ionosphere resulting in modulation of the phase and amplitude of the signal.

The signal received by a SAR from a point target, after compensating for the satellite motion and performing the usual SAR processing [*Oliver and Quegan*, 2004], can be written as

$$S(x) = A(x)\exp\{i\Psi(x)\}. \tag{6}$$

Here $\Psi(x)$ is the residual phase modulation over the synthetic aperture due to the ionosphere (zero for a perfectly focussed image) and $A(x)$ is the amplitude modulation over the aperture due to the ionosphere. The PSF can then be represented as the Fourier transform of this function:

$$\mathrm{PSF} = \mathcal{F}\{A(x)\exp\{i\Psi(x)\}W(x)\} \tag{7}$$

where $W(x)$ is a window function to reduce sidelobes (and with the consequential trade-off of widening the main lobe). If there are no ionospheric effects and no window function, the processed signal from a point target will be a top-hat function, and hence, its PSF will be described by a sinc function.

2.4. Synthesizing the SAR PSF Using GPS Data

This paper proposes an alternative to measuring the PSF from a radar signal, that is, to synthesize the PSF using GPS carrier phase and amplitude data. First, in order to derive an equivalent SB-SAR PSF from GPS data, it is necessary to double the measured phase and square the amplitude in order to compensate for the fact that the GPS signal only passes once through the ionosphere. In so doing, it is assumed that the down and up legs of the propagation path are perfectly correlated [*Rogers et al*., 2009].

Second, the GPS phase must be detrended. This is an important practical problem because the movement of the satellite introduces phase changes of many thousands of radians which mask the effects of the irregularities. Fortunately, because SAR processing removes (through a matched filter) the quadratic component of phase introduced by the satellite motion, the second-order terms in the GPS carrier phase can be removed (using a polynomial fit in our processing). Constant and linear terms can also be removed as these terms are caused by the bulk ionosphere, rather than the smaller-scale irregularities.

Defining the detrended and doubled GPS phase data as Ψ_{DT} and the two-way amplitude modulation derived from the one-way GPS amplitude (i.e., the square) as $A_{2\mathrm{GPS}}(t)$ the synthesized signal derived from the GPS data can be written as

$$S(t) = A_{2\mathrm{GPS}}(t)\ \exp[i\Psi_{\mathrm{DT}}(t)]. \tag{8}$$

$S(t)$ is equivalent to the SAR signal from a point target. The SAR along-track PSF is then given by applying equation (9):

$$\mathrm{PSF} = \mathcal{F}\{\ A_{2\mathrm{GPS}}(t)\ \exp[i\Psi_{\mathrm{DT}}(t)W(t)]\}, \tag{9}$$

where $W(t)$ has been chosen to be a Hamming window function.

Rather than determine the one-way carrier phase directly from the signal, it was indirectly calculated by differencing the L1 and L2 phases (the geometry-free combination) to give the slant total electron content (STEC). This approach removes many of the unwanted errors common to both frequencies. The corresponding ionospheric component of the carrier phase is then given by [*Hofmann-Wellenhof et al*., 1997]:

$$\Psi = \frac{8.44\times10^{-7}}{f}\mathrm{STEC}_{\Phi}\ (\mathrm{radians}). \tag{10}$$

This paper only addresses ionospheric phase effects and consequently the amplitude has been set to unity in the following analysis.

2.5. Practical Considerations

2.5.1. GPS Analysis Period

The analysis period of the GPS signal data was chosen to ensure that the distance traveled by the GPS IPP properly corresponds to the length of a typical PALSAR-2 synthetic aperture (L_{SA}) projected to ionospheric height (L_C). This is the distance moved by the SAR IPP along the phase screen as the radar traverses the synthetic aperture L_{SA} and is the distance over which signal coherency is required. These two quantities can be written as

$$L_{\mathrm{SA}} = \gamma L_C, \tag{11}$$

where γ is the ratio between the SAR velocity and the effective velocity in the ionosphere. It accommodates the height difference between SAR and ionosphere and anisotropy of the ionospheric irregularities

Figure 1. Ascension Island (7.9°S, 14.8°W showing the ESA Tracking Station which was the location of the fixed receiver and the road (shown in black) along which the mobile measurements were made).

[*Belcher and Cannon*, 2014]. A SB-SAR, such as PALSAR-2 in LEO at an altitude of ~700 km, is at approximately twice the height of the ionosphere *F* region peak (the assumed height of the phase screen). Consequently, for an isotropic ionosphere $\gamma = 2$. However, if due allowance is made both for the anisotropy of the irregularities and the PALSAR-2 orbit, $\gamma = 3$ is a better approximation while imaging Ascension Island. Consequently, the required ionospheric coherence length for this study is one third that of the synthetic aperture length.

For a SAR operating in strip-map mode:

$$L_{SA} = \frac{R_0 \lambda}{2\rho_{az}}, \tag{12}$$

where ρ_{az} is the along-track resolution, R_0 is the broadside slant range to the target, and λ is the carrier wavelength. For PALSAR-2, at a typical broadside slant range of 847 km, a maximum along-track resolution of 2 m and a wavelength at the center frequency of 1270 MHz, the maximum synthetic aperture (L_{SA}) is ~50 km and it follows that $L_c = 17$ km.

The velocity of the GPS IPP combined with the distance L_c gives the duration of the corresponding GPS data block which will be analyzed. GNSS satellites, in medium Earth orbit, have IPP velocities that depend heavily on the elevation and azimuth angles of the satellite to the receiver. For GPS at an elevation angle of 40°, IPP velocities in an east-west/west-east direction of 26–37 m s^{-1} are typical [*Forte and Radicella*, 2002]. However, the pertinent velocity in this analysis is the effective velocity, being the vector addition of the IPP velocity, due to the satellite motion, and the ionospheric drift speed. As the latter is typically 100 m s^{-1} (west to east) in the premidnight sector, it is the dominant velocity component.

For the purposes of this analysis the effective IPP velocity has been fixed at 100 m s^{-1} west-east representing a reasonable average between lower and higher values. Clearly, this will introduce some errors, but without recourse to well-validated measurement data, it is considered a reasonable approximation. It follows that 170 s (180 s was used in practice) of GPS data is required to synthesize a 2 m resolution image by PALSAR-2 of Ascension Island ($L_c = 17$ km).

Of course correspondingly, shorter and longer data sets can be used to synthesize smaller and larger synthetic apertures. It is important to note that SB-SAR in LEO has an IPP velocity of ~3700 m s^{-1} and takes <3 s to scan 10 km along the ionospheric phase screen. The time-evolving ionospheric structure can thus be considered frozen in. In contrast, GPS data blocks of hundreds of seconds will mix temporal and spatial effects.

3. Experiment

GPS data were recorded on Ascension Island in the South Atlantic, (7.9°S, 14.8°W, magnetic latitude −16°) (Figure 1). Ascension Island lies in the ionospheric equatorial region where small- and medium-scale electron density irregularities are likely to occur between 21 local time (LT) and 00 LT [*Aarons*, 1982]. Data were collected during the period 25 to 31 January 2013 and 20 to 30 January 2014.

Two Septentrio PolaRx4 PRO GNSS receivers were used to collect the data, with each locked to a rubidium oscillator to ensure stability. One was located at the European Space Agency (ESA) Tracking Station on the

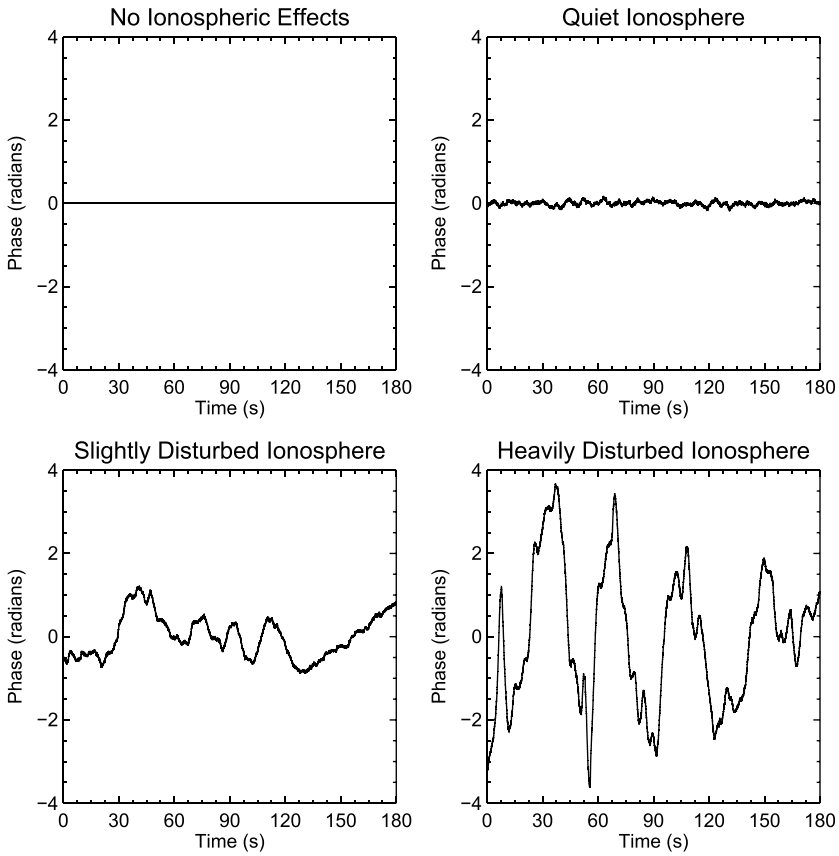

Figure 2. Examples of the residual phase modulation for quiet and disturbed ionospheric conditions as recorded by the GPS receivers on Ascension Island.

northeastern coast of the island (marked on the map in Figure 1), while the other was moved to various locations at distances ranging from ~100 to 9000 m along an approximate (dictated by road access and marked with a black line in Figure 1) magnetic east-west axis with the ESA station. This axis was chosen as it lies in the direction of minimum irregularity correlation (the irregularities are assumed to be aligned with, and elongated along, the magnetic field lines) and parallel to the *F* region drift direction [*Aarons*, 1982]. The signal phase and amplitude were recorded at 50 Hz. To minimize multipath effects and minimize the horizontal spatial separation of the GPS L1 and L2 signals, only data from satellites above an elevation angle of 40° were considered. Only data without cycle slips were analyzed.

4. Single Location Results

4.1. Point Spread Functions

The proxy (detrended) signal phase from four 180 s (9000 samples at 50 Hz sampling rate) blocks of GPS data with contrasting levels of ionospheric effect is shown in Figure 2, and the effect of the phase modulation on the shape of the PSF is illustrated in Figure 3. Figures 2 and 3 (top left) show artificially generated test data that correspond to no ionospheric effects, and so the shape of Figure 3 (top left) is dictated by the windowing function. The Hamming window provided a PSLR of 42 dB.

Figure 3 (top right) shows the PSF corresponding to very small phase variations of 0.05 rad RMS in Figure 2 (top right). These phase variations are considered likely due to receiver noise, not ionospheric scintillation, as the signals were completely uncorrelated between two receivers. The sidelobes close to the main lobe are raised slightly and drop off more gradually than the ideal (Figure 3, top left).

The phase variations produced by the disturbed ionosphere (Figure 2, bottom left (0.50 rad RMS) and bottom right (1.65 radians RMS)) have a more severe effect on the PSF (Figure 3, bottom left and bottom right) and

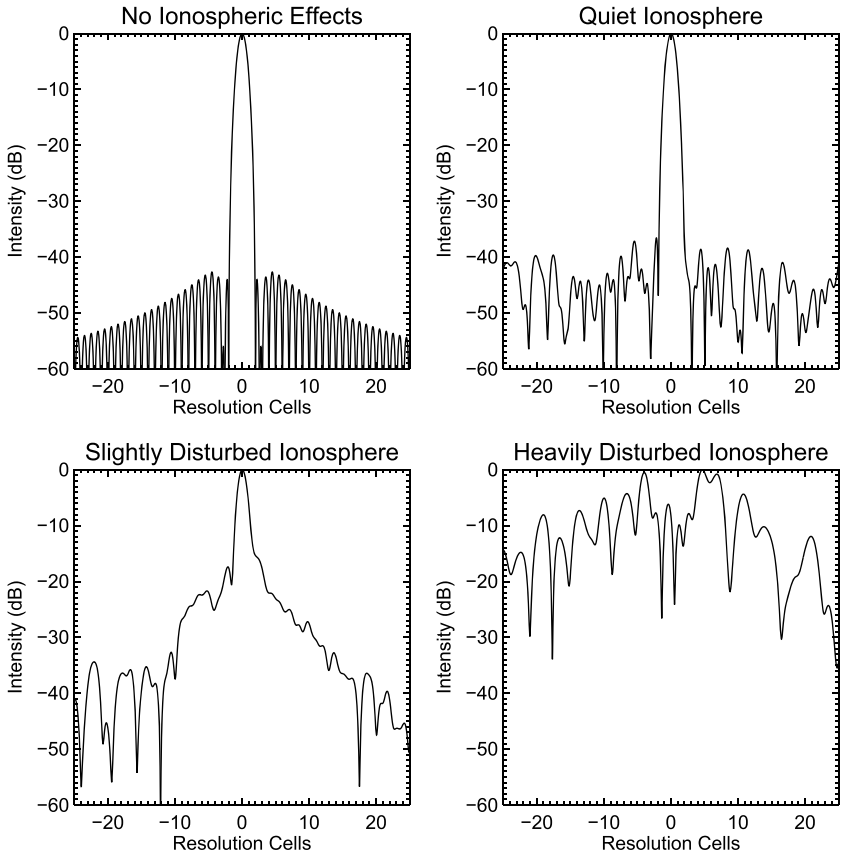

Figure 3. Point spread functions for different levels of ionospheric disturbance, generated from GPS signal data recorded on Ascension Island.

are due to ionospheric scintillation. The terms "slightly" and "heavily" are indicative and based on the RMS phase. Figure 3 (bottom left) still retains an obvious main lobe, but the sidelobes closest to the main lobe have been raised significantly leading to a PSLR of only 18 dB (although the sidelobes more than 10 resolution cells away from the center of the PSF are only slightly raised compared to those of Figure 3, top right). The low PSLR indicates that the contrast of a SAR image of this point would be reduced. The phase variations shown in Figure 2 (bottom right) correspond to the heavily distorted PSF shown in Figure 3 (bottom right). There is no main lobe in the PSF, and therefore, the point target would be obscured in the image. The lack of main lobe means that the PSLR ceases to be a sensible metric for the PSF, and in cases like this, it was set to zero for subsequent analysis.

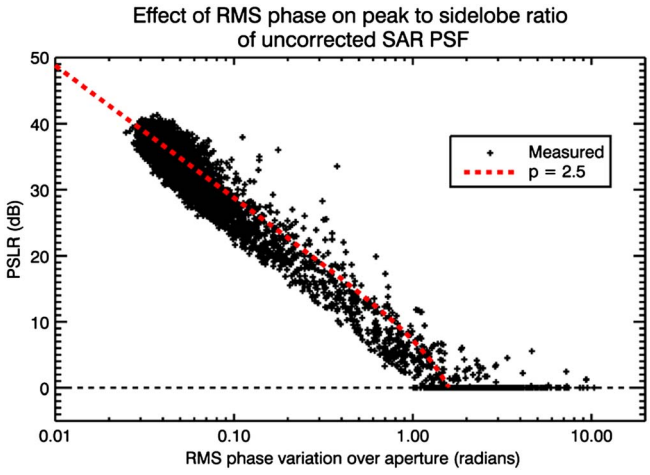

Figure 4. Relationship between RMS phase and PSLR.

Nearly 2400 point spread functions were produced from the GPS data, collected from multiple satellites on both receivers, during a wide variety of ionospheric conditions. The variation of the PSLR with RMS phase variation over the 180 s apertures is shown in Figure 4. The PSLR decreases with increasing RMS phase values, and above ~0.5 rad the PSLR is sufficiently low that few details would be visible in an image.

Belcher and Rogers [2009] described an analytical form for the ensemble average

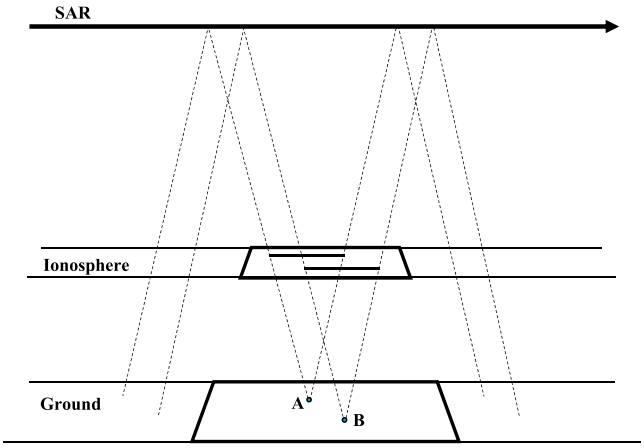

Figure 5. Geometry of SAR signals and the ionospheric phase screen for two points in the image. Dashed lines illustrate the real beam width.

SAR PSF which has been degraded by ionospheric irregularities lying in a single phase screen. They provided expressions for the effect of phase scintillation on the sidelobes (the sidelobe function or SLF) and the peak of the main lobe, as a function of the RMS phase ϕ_{RMS} at the phase screen. This theory has been adapted to fit the data in Figure 4.

For a given ϕ_{RMS}, the sidelobe intensity, as a function of distance from the main lobe in resolution cells r (where the main lobe is located at $r=1$), is given by

$$\left\langle |\mathrm{SLF}(r)|^2 \right\rangle = 2\gamma r^{-p}(p-1)\phi_{\mathrm{RMS}}^2, \quad (13)$$

and the main lobe peak intensity is

$$\mathrm{MLP} = \left(1 - 2\phi_{\mathrm{RMS}}^2\right)^2. \quad (14)$$

The first measurable sidelobe is located at $r=2$, as the sidelobe at $r=1$ is obscured by the main lobe. Assuming that this is the largest, the peak-to-sidelobe ratio is

$$\mathrm{PSLR} = \mathrm{MLP}\left\langle |\mathrm{SLF}(2)|^2 \right\rangle. \quad (15)$$

However, in this study the relevant RMS phase is that at the synthetic aperture, rather than in the phase screen. To address this, we recall that the RMS phase in the phase screen is determined by integrating over the phase power spectrum:

$$\phi_{\mathrm{RMS}}^2 = 2\int_{\kappa_c}^{\infty} \mathrm{PSD}_{\phi}(\kappa)\mathrm{d}\kappa, \quad (16)$$

where κ is the associated spatial wave number and $\kappa_C = {}^{2\pi}\big/ L_C$, where L_C is the phase screen coherence length required to form a coherent synthetic aperture.

Belcher and Rogers [2009] show that the SLF can be calculated as

$$\left\langle |\mathrm{SLF}(r)|^2 \right\rangle = 4\gamma\kappa_c \mathrm{PSD}_{\phi}(\kappa)|_{\kappa=r\kappa_c}, \quad (17)$$

and by integration and using (16),

$$2\int_1^{\infty} \left\langle |\mathrm{SLF}(r)|^2 \right\rangle \mathrm{d}r = 4\gamma\phi_{\mathrm{RMS}}^2. \quad (18)$$

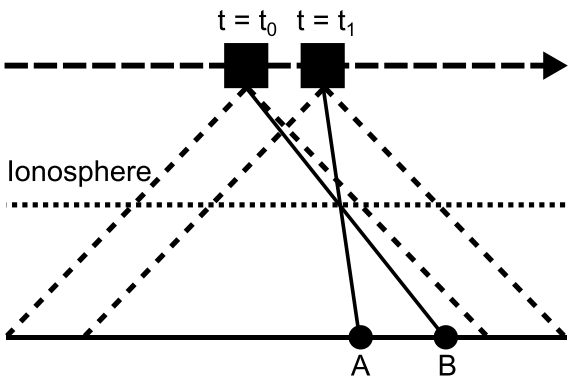

Figure 6. Differences in SAR signal paths in the along-track direction.

Alternatively, the SLF can be considered a function of the phase at the synthetic aperture. The latter is determined by the Fourier transform of the phase variations received at the SAR synthetic aperture with power conserved. Thus, the integral over the square of the sidelobe function is also equal to the square of the RMS phase values received at the aperture, ψ_{RMS}^2.

$$2\int_1^{\infty} \left\langle |\mathrm{SLF}(r)|^2 \right\rangle \mathrm{d}r = \psi_{\mathrm{RMS}}^2. \quad (19)$$

It follows from equations (18) and (19) that

$$\psi_{\mathrm{RMS}}^2 = 4\gamma\phi_{\mathrm{RMS}}^2. \quad (20)$$

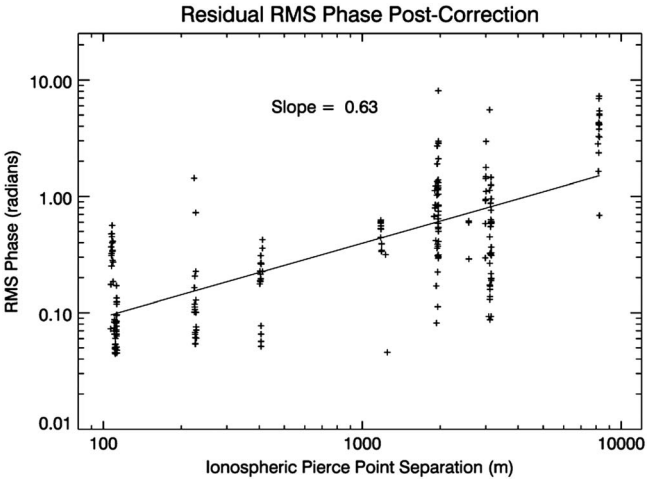

Figure 7. RMS phase difference (for precorrection PSLR <5 dB).

Here the factor of 4 is a consequence of the two-way path of the signal at the aperture and gamma has been previously defined. (It is worth noting that experimentally, the integrations in (18) and (19) can only be performed from the first measurable sidelobe. The derivation of (20) is, however, not constrained by practical limitations.)

It follows from (20) that in terms of the phase variations at the synthetic aperture

$$\mathrm{MLP} = \left(1 - \frac{\psi^2_{\mathrm{RMS}}}{2\gamma}\right)^2, \tag{21}$$

and

$$\left\langle |\mathrm{SLF}(2)|^2 \right\rangle = 2^{-p-1}(p-1)\psi^2_{\mathrm{RMS}}. \tag{22}$$

Consequently, the PSLR is

$$\mathrm{PSLR}\ (\mathrm{d}B) = 10\log_{10}\left[\frac{2\left(1 - \frac{\Psi^2_{\mathrm{DT}}}{2\gamma}\right)^2}{2^{-p}(p-1)\Psi^2_{\mathrm{DT}}}\right], \tag{23}$$

where ψ^2_{RMS} has been replaced by the detrended GPS RMS phase Ψ^2_{DT}, being a good estimate of ψ^2_{RMS}.

Setting $\gamma = 3$, being appropriate to PALSAR-2 imaging Ascension Island, and p to a typical value of 2.5 [*Basu et al.*, 1987; *Carrano and Groves*, 2010], provides a good fit to the data in Figure 4. This provides confidence in the GPS proxy approach.

5. Two Location Results

5.1. Variation in RMS Phase Difference With Distance

Techniques to correct ionospheric distortion from small-scale irregularities which affect SB-SAR might be achieved by measuring the signal from a point target, for example, a corner reflector (CR). Assuming that the response from the CR dominates the return from its resolution cell, then, after performing the SAR processing, the phase history of the signal across the synthetic aperture is a measure of the ionospheric impact. This estimate might then be applied to mitigate the ionospheric degradation at other locations in the image.

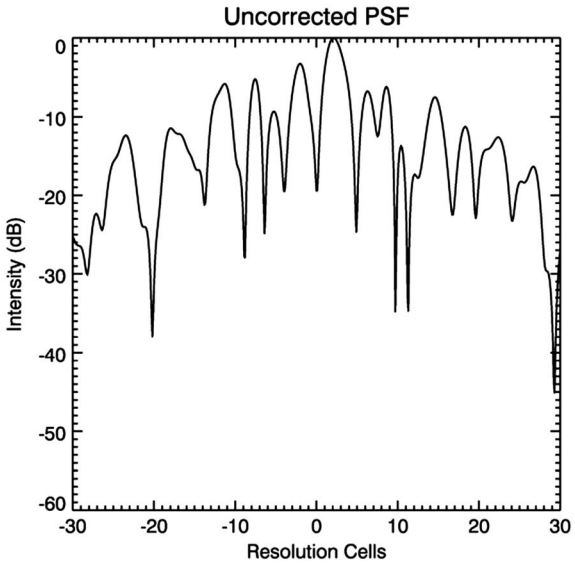

Figure 8. Uncorrected PSF, SVID 29, 26 January 2014.

Applying a phase correction derived from one location to the phase received from another location separated in the range and the along-track directions requires careful consideration of the geometry (see Figure 5 for a SAR in strip-map mode). For points sufficiently close (in the along-track direction) the IPP tracks overlap and the signals are received simultaneously. It follows that a correction can be achieved by aligning the CR calibration signal with the signal from the remote location. Figure 6 describes a simplified, one-dimensional example where the solid diagonal lines describe the signal paths from two points within the real antenna beam (denoted by the dashed lines). In this

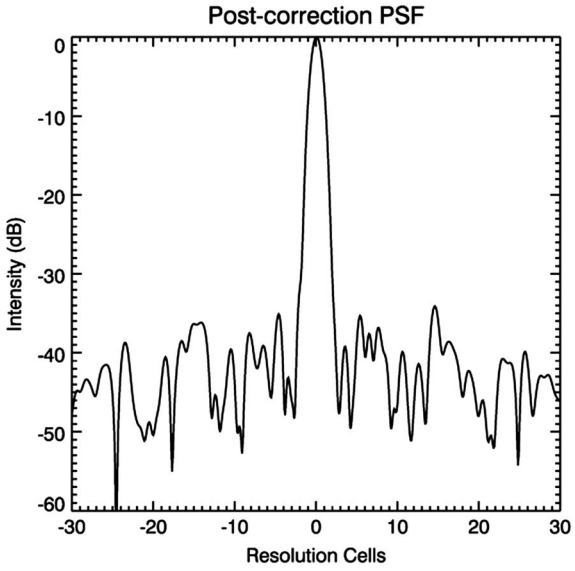

Figure 9. Postcorrection PSF (receiver separation ~250 m). SVID 29, 26 January 2014.

example the signal from location A received by the SAR at time t_1 intersects the ionosphere at the same IPP as that from location B at time t_0. Thus, to properly correct the signal from location A received at t_1, the phase correction from point B at t_0 must be used. The use of this time offset effectively aligns the two signals spatially, allowing the correction to be performed.

In Figure 5 the IPP tracks do not fully overlap in the along-track direction (the general case) and only a portion of the signal can be corrected. However, a series of corner reflectors separated by a fraction (determined by the ratio of the phase screen height to the radar height) of the real radar beam width in the along-track direction would provide a continuous series of phase corrections in the along-track direction.

The same geometry issues also apply to the GPS data, where the points "A" and "B" from Figure 5 are analogous to the GPS receivers. The two GPS receiver data sets were aligned by cross correlation, with the peak correlation giving the along-track time offset between the two. Writing the sample-by-sample phase difference between the two data sets as

$$\text{Phase Difference } = \Psi^{\alpha}_{\text{DT}}(t) - \Psi^{\beta}_{\text{DT}}(t + \Delta t), \tag{24}$$

the RMS phase difference (over 180 s) at a range of IPP separations was determined (Figure 7).

As expected there is a general upward trend in the residual RMS phase postcorrection as the IPP separation increases—although at each separation there are a wide spread of values. This may be a result of differences in the GPS IPP scan length due to errors in the assumed scan velocity, or due to the data being collected at different times with correspondingly different strengths of turbulence (see equation (4)), or due to different phase power law indices. Noting that the two GPS receivers were deployed along an approximate magnetic east-west axis, the experiment provides a worst-case estimate of the distance dependence of the phase correction.

The average RMS value at each distance follows the form given in equation (4), i.e., a linear relationship with a (log-log) slope of $\frac{1}{2}(p-1)$. The least squares slope (the solid line in Figure 7) is 0.64, corresponding to a phase spectral index value of $p = 2.28$, close to the expected value of $p = 2.5$.

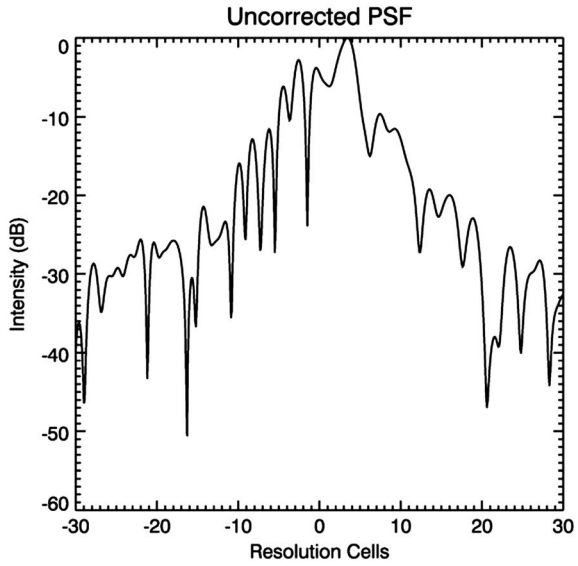

Figure 10. Uncorrected PSF, SVID 29, 24 January 2014.

5.2. Sharpening the PSF

The proxy data can now be used to determine the benefits of using measurements at one location (β) to correct the phase at another location (α).

The corrected PSF can be written as

$$\text{PSF}(s) = \mathcal{F}\{A^{\alpha}_{\text{2GPS}}(t)\ \exp[i(\ \Psi^{\alpha}_{\text{DT}}(t) - \Psi^{\beta}_{\text{DT}}(t + \Delta t))]\}, \tag{25}$$

where $\Psi^{\alpha}_{\text{DT}}(t)$ is the phase block recorded at the primary receiver and $\Psi^{\beta}_{\text{DT}}(t + \Delta t)$ is the phase recorded at the secondary receiver, offset by the peak correlation lag.

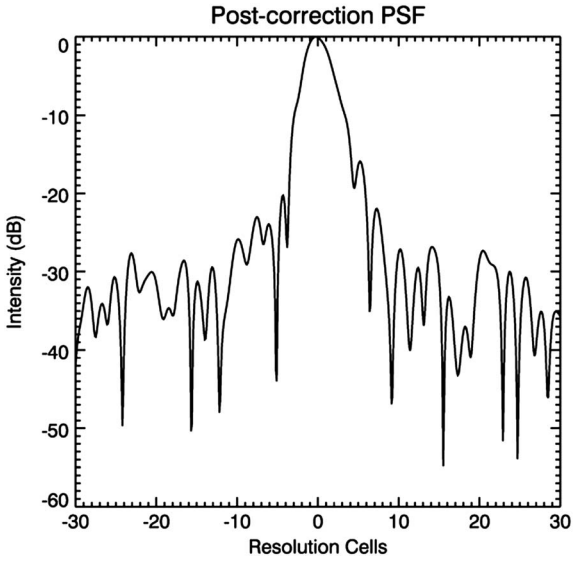

Figure 11. Postcorrection PSF (receiver separation ~2500 m). SVID 29, 24 January 2014.

Two examples of the effect of applying this phase correction on the PSF are shown in Figures 8–11. The first pair of plots (Figures 8 and 9) shows the precorrection and postcorrection PSFs, respectively, with the correction performed using data collected with the secondary receiver only ~250 m away from the primary receiver. Figure 8 shows a heavily distorted PSF, with no main lobe at all, in a similar manner to Figure 3 (bottom right). Despite this, the phase correction is very effective, restoring a narrow main lobe and drastically reducing the level of the sidelobes to ~38 dB down from the main lobe.

The latter pair (Figures 10 and 11) shows the impact of performing the correction using more widely spaced receivers. In this case, the correction is performed using data collected at a separation of ~2500 m. It can be seen that for a similarly disturbed precorrection PSF (compared to the previous example), the correction is less effective. The main lobe is much wider, and the peak sidelobes either side of the main lobe are only ~20 dB down.

The degree of benefit is dependent on many factors, but Figure 12 shows the impact of applying the correction on apertures that have been heavily affected by the ionosphere (defined as having a PSLR of less than 5 dB), as a function of signal separation in the ionosphere.

The greatest benefits (30 dB) are seen at the smallest IPP separations with decreasing benefit (10 dB) out to IPP distances of ~3 km. Again, there is large variability which is likely driven by different ionospheric conditions. Notwithstanding the variability in benefit, the correction consistently improves the PSLR and rarely does the application of the reference phase correction degrade the PSF and, therefore, the associated image. A least squares fit shows that the benefit decreases at 13.0 dB per decade (in distance).

6. Conclusions

A method has been described which utilizes L-band GPS amplitude and phase data as a proxy for L-band space-based synthetic aperture radar (SB-SAR) signals. This is further developed to synthesize the equivalent SAR point spread function (PSF).

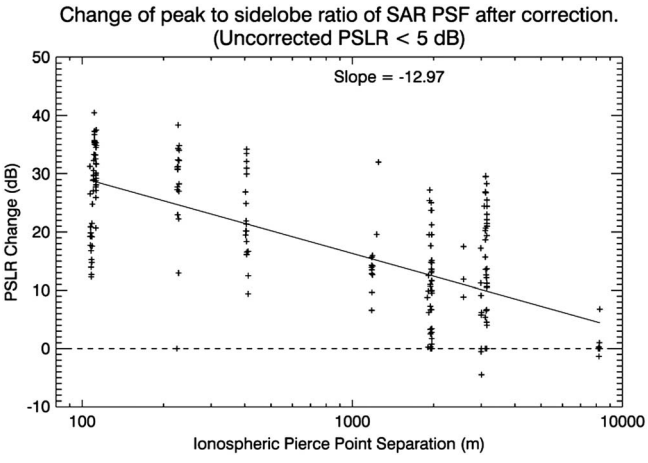

Figure 12. PSLR change after phase correction for uncorrected PSF PSLR <5 dB.

The technique has been tested using measurements at a single location, and the synthesized peak-to-sidelobe ratio (PSLR) has been shown to approximately follow the expected weak scattering theory variation with RMS phase. Then, using two position measurements, the synthesized SB-SAR RMS phase has been shown to exhibit spatial characteristics which are consistent with a phase screen, again described by the weak scattering theory. These tests provided confidence in the SB-SAR synthesis technique.

Using the synthesized L-band SAR PSF, the viability of correcting the phase recorded at one location using the

phase recorded at another was investigated. This was achieved by exploring whether the ionospheric GPS phase (after the geometric terms had been subtracted) at one location could be used to improve the PSF at another location. This was quantified in terms of the difference between the PSLR of the precorrection PSF and the PSLR of the postcorrection PSF. At short distances (i.e., 100 m between IPP points) the benefit was ~30 dB, but this fell to around 10 dB at an IPP separation of 3000 m. An IPP separation of 3000 m corresponds to a ground range of ~6000 m for a LEO L-band SB-SAR. Consequently, these results suggest that ionospheric mitigation techniques based upon a reference corner reflector would be effective in improving an L-band SAR image at ground separations up to 6000 m.

Acknowledgments
The authors wish to acknowledge the work of Stephen White who has spent many weeks on Ascension Island installing and contributing to the running of this equipment. The GNSS signal data (in RINEX format) may be obtained by contacting the corresponding author at p.cannon@bham.ac.uk.

References

Aarons, J. (1982), Global morphology of ionospheric scintillations, *Proc. IEEE*, *70*(4), 360–378, doi:10.1109/proc.1982.12314.
Aarons, J., M. Mendillo, R. Yantosca, and E. Kudeki (1996), GPS phase fluctuations in the equatorial region during the MISETA 1994 campaign, *J. Geophys. Res.*, *101*(A12), 26,851–26,862, doi:10.1029/96JA00981.
Basu, S., E. MacKenzie, E. Costa, P. Fougere, H. Carlson, and H. Whitney (1987), 250 MHz/GHz scintillation parameters in the equatorial, polar, and auroral environments, *IEEE J. Selec. Areas Commun.*, *5*(2), 102–115, doi:10.1109/JSAC.1987.1146533.
Belcher, D. P., and N. C. Rogers (2009), Theory and simulation of ionospheric effects on synthetic aperture radar, *IET Radar Sonar Navig.*, *3*(5), 541–551, doi:10.1049/iet-rsn.2008.0205.
Belcher, D. P., and P. S. Cannon (2014), Amplitude scintillation effects on SAR, *IET Radar Sonar Navig.*, *8*, doi:10.1049/iet-rsn.2013.0168.
Belcher, D. P., P. S. Cannon, and A. Gustavsson (2015), The Ascension Island experiment: Measurement of ionospheric scintillation effects on PALSAR2, in *International Geoscience and Remote Sensing Symposium 2015 (IGARSS 2015)*, 3191–3194, doi:10.1109/IGARSS.2015.7326496, IEEE, Milan, Italy, 26–31 July.
Cannon, P. S. (2009), Mitigation and exploitation of the ionosphere: A military perspective, *Radio Sci.*, *44*, 1–8, doi:10.1029/2008RS004021.
Carrano, C., and K. Groves (2010), Temporal decorrelation of GPS sateliite signals due to multiple scattering from ionospheric irregularities, in *23rd International Technical Meeting of the Satellite Division of the Institute of Navigation*, pp. 21–24, ION, Portland, Oreg.
Forte, B., and S. M. Radicella (2002), Problems in data treatment for ionospheric scintillation measurements, *Radio Sci.*, *37*(6), 5–8, doi:10.1029/2001RS002508.
Freeman, A. (1992), SAR calibration: An overview, *IEEE Trans. Geosci. Remote Sens*, *30*(6), 1107–1121, doi:10.1109/36.193786.
Hofmann-Wellenhof, B., H. Lichtenegger, and J. Collins (1997), *Global Positioning System: Theory and Practice*, 4th ed., Springer, Wien, Austria.
Kankaku, Y., S. Suzuki, and Y. Osawa (2013), ALOS-2 mission and development status, *Int. Geosci. Remote Sens. Symp.*, 2396–2399, doi:10.1109/IGARSS.2013.6723302.
Knepp, D. L. (1983), Multiple phase-screen calculation of the temporal behavior of stochastic waves, *Proc. IEEE*, *71*(6), 722–737, doi:10.1109/PROC.1983.12660.
Knepp, D. L., and K. M. Groves (2011), The effect of ionospheric scintillation on phase gradient autofocus processing of synthetic aperture radar, in *URSI XXXth General Assembly and Scientific Symposium*, doi:10.1109/ursigass.2011.6050878, Istanbul, 13–20 Aug. 2011.
Meyer, F. J., and J. B. Nicoll (2008), Prediction, detection, and correction of Faraday rotation in full-polarimetric L-band SAR data, *IEEE Trans. Geosci. Remote Sens.*, *46*(10), 3076–3086, doi:10.1109/TGRS.2008.2003002.
Oliver, C., and S. Quegan (2004), Principals of SAR image formation, in *Understanding Synthetic Aperture Radar Images*, pp. 11–42, SciTech Publ., Raleigh, N. C.
Pi, X., A. J. Mannucci, U. J. Lindqwister, and C. M. Ho (1997), Monitoring of global ionospheric irregularities using the Worldwide GPS Network, *Geophys. Res. Lett.*, *24*(18), 2283–2286, doi:10.1029/97GL02273.
Quegan, S., and J. Lamont (1986), Ionospheric and tropospheric effects on synthetic aperture radar performance, *Int. J. Remote Sens.*, *7*(4), 525–539, doi:10.1080/01431168608954707.
Rino, C. L. (1979), A power law phase screen model for ionospheric scintillation: 1. Weak scatter, *Radio Sci.*, *14*(6), 1135–1145, doi:10.1029/RS014i006p01135.
Rino, C. L. (1982), On the application of phase screen models to the interpretation of ionospheric scintillation data, *Radio Sci.*, *17*(4), 855–867, doi:10.1029/RS017i004p00855.
Rino, C. L., and V. H. Gonzalez (1983), Propagation effects in satellite-borne synthetic aperture radars, in *Propagation Factors Affecting Remote Sensing by Radio Waves*, 345, 5-1 to 5-12, NATO-AGARD, Electromagnetic Propagation Panel (EPP), Oberammergau, Federal Republic of Germany, 18-24 May.
Rogers, N. C., P. S. Cannon, and K. M. Groves (2009), Measurements and simulation of ionospheric scattering on VHF and UHF radar signals: Channel scattering function, *Radio Sci.*, *44*, 1–10, doi:10.1029/2008RS004033.
van de Kamp, M., P. S. Cannon, and M. Terkildsen (2009), Effect of the ionosphere on defocusing of space-based radars, *Radio Sci.*, *44*, RS1003, doi:10.1029/2007RS003808.
Vexcel Corporation (2003), PALSAR algorithm description—VX-PALSAR-010 v1.0, Boulder, Colo.
Xu, Z.-W., J. Wu, and Z.-S. Wu (2004), A survey of ionospheric effects on space-based radar, *Waves Random Media*, *14*(2), S189–S273, doi:10.1088/0959-7174/14/2/008.
Yeh, K. C., C. H. Liu, and M. Y. Youakim (1975), A theoretical study of the ionospheric scintillation behavior caused by multiple scattering, *Radio Sci.*, *10*(1), 97–106, doi:10.1029/RS010i001p00097.